Effect of Recycled Pet-GFRP Hybrid Laminates on the Ultimate Moment Capacity of Reinforced Concrete Beams

M. G. Bah[1*], N. Gathimba[2], S. O. Abuodha[3]

[1]Department of Civil Engineering, Pan African University, Institute of Basic Sciences Technology and Innovation, Nairobi, Kenya

[2]Department of Civil, Construction and Environmental Engineering, Jomo Kenyatta University of Agriculture and Technology (JKUAT), Nairobi, Kenya

[3]Department of Civil Engineering, University of Nairobi, Nairobi, Kenya

ABSTRACT: Reinforced concrete (RC) structures increasingly require strengthening due to ageing, deterioration, and higher service demands. Conventional glass fibre-reinforced polymer (GFRP) strengthening systems effectively improve flexural strength but exhibit brittle failure and limited deformation capacity, while sustainable alternatives capable of balancing strength and ductility remain insufficiently investigated. The objective of this study was to evaluate the influence of recycled polyethylene terephthalate fibre-reinforced polymer (PET-FRP) and GFRP hybrid laminate configurations and stacking sequence on the flexural performance of RC beams. Ten under-reinforced RC beams (150 × 250 × 1200 mm) were cast using C30 concrete and divided into five groups comprising an unstrengthen control, PET-FRP, GFRP, PET-GFRP-PET, and GFRP-PET-GFRP strengthening configurations. Tensile coupon tests were conducted to determine the mechanical properties of the laminates before they were externally bonded to the beam soffits using Sikadur®-30 epoxy through the wet lay-up technique. All specimens were tested under four-point monotonic bending, and load-deflection response, ultimate moment capacity, displacement ductility, strain development, and failure modes were evaluated. The GFRP-PET-GFRP hybrid configuration achieved the highest ultimate moment capacity of 38.57 kN·m, representing a 57.6% increase over the control beam, while the PET-GFRP-PET hybrid attained 36.67 kN·m with superior hybrid ductility ($\mu = 3.36$). PET-FRP-only beams exhibited the greatest ductility ($\mu = 3.96$), whereas GFRP-only beams showed the lowest ductility because of brittle fibre rupture. Both hybrid laminates exhibited progressive failure mechanisms that enhanced structural performance compared with the single-material systems. These findings demonstrate that recycled PET-GFRP hybrid laminates provide an effective and sustainable strengthening solution for RC beams. The GFRP-PET-GFRP configuration is recommended where maximum flexural strength is required, whereas the PET-GFRP-PET configuration is more suitable for applications requiring greater deformation capacity.

KEYWORDS: PET-GFRP hybrid laminates, moment capacity, stacking sequence, ductility index, sustainable retrofitting

[Received May 01, 2026; Revised May. 09, 2026; Accepted May 12, 2026] Print ISSN: 0189-9546 | Online ISSN: 2437-2110

I. INTRODUCTION

Reinforced concrete (RC) structures constitute the backbone of global civil infrastructure, yet a significant proportion of existing stock suffers degradation due to ageing, corrosion of reinforcement, environmental exposure, and escalating service demands beyond original design capacities (Hollaway, 2010). Structural rehabilitation using externally bonded fibre-reinforced polymer (FRP) composites has emerged as a leading intervention strategy, offering high tensile strength, low self-weight, corrosion resistance, and ease of application with minimal disruption to occupants (Hollaway, 2010; American Concrete Institute, 2017; Siddika et al., 2019; Naser et al., 2019). Siddika et al. (2019) and Naser et al. (2019) provided comprehensive reviews confirming that FRP strengthening consistently enhances flexural capacity, though the degree of enhancement depends strongly on fibre type, laminate configuration, and bond quality. Teng et al. (2002) established the foundational design principles for FRP-strengthened RC structures, which have been adopted and refined in subsequent international design guidelines (American Concrete Institute, 2017; Nanni, 2003).

Despite these advantages, conventional FRP systems including carbon FRP (CFRP), glass FRP (GFRP), and aramid FRP (AFRP) exhibit a characteristically linear-elastic stress-strain response to brittle rupture, with ultimate strains typically below 2% (Hollaway, 2010; Bakis et al., 2002). When applied as flexural strengthening, GFRP laminates enhance moment capacity by 30-45% but result in abrupt, brittle failure modes with limited post-yield deformation and energy absorption (Saadatmanesh and Ehsani, 1991; Attari et al., 2012; Alsayed

*Corresponding author: *bah.mohamed@students.jkuat.ac.ke*

doi: http://doi.org/10.63746/njtd.v23i2.4716

et al., 2000). Saadatmanesh and Ehsani (1991) provided one of the earliest systematic experimental studies on GFRP-strengthened RC beams, reporting strength enhancements of up to 40% but with significantly reduced ductility compared to unstrengthen controls. This brittleness is particularly problematic in seismic regions and in structures where controlled deformation is essential for occupant safety, warning before collapse, and structural redundancy (Dai et al., 2011; Bai et al., 2014; Elchalakani and Karrech, 2017). Furthermore, CFRP and GFRP systems are expensive, energy-intensive to produce, and non-recyclable, limiting their applicability in low-resource settings and sustainability-focused projects (Bai et al., 2024; Monteiro et al., 2017).

Recycled PET fibre-reinforced polymer (PET-FRP), a representative example of the broader class of large-rupture-strain composites, offers a fundamentally different material response: rupture strains exceeding 7% (approximately three to five times greater than conventional FRPs) and pronounced bilinear stress-strain behaviour (Dai et al., 2011; Bai et al., 2014; Bai et al., 2024; Hawileh et al., 2022). Dai et al. (2011) provided the first comprehensive characterisation of the bilinear constitutive behaviour of PET-FRP and demonstrated its effectiveness in confinement applications, while Bai et al. (2014) extended this work to cyclic compressive loading conditions. Hawileh et al. (2022) demonstrated that two PET-FRP layers achieved 47% strength enhancement over unstrengthen beams with 33% greater ductility than an equivalent CFRP system. Bai et al. (2024) confirmed high-energy absorption and superior ductility in hybrid carbon-PET FRP-strengthened beams.

The sustainable use of recycled PET in construction materials has gained increasing attention. Frigione (2010) demonstrated that recycled PET from waste bottles could be successfully incorporated into concrete and FRP applications without significant loss of mechanical properties, while Pacheco-Torgal et al. (2012) provided an overview confirming that polymeric wastes including PET and tyre rubber exhibit adequate durability for structural applications when properly processed. These studies establish the circular-economy credentials of recycled PET-FRP as a strengthening material (Monteiro et al., 2017; Frigione, 2010; Pacheco-Torgal et al., 2012). Reis and Ferreira (2004) further demonstrated that polymer concrete reinforced with glass and carbon fibres exhibits excellent fracture properties, supporting the broader application of fibre-reinforced polymer systems in civil infrastructure.

While the hybridisation of carbon FRP and PET-FRP into single externally bonded laminates has been investigated by Bai et al. (2024) and Hawileh et al. (2014), the combination of glass FRP with recycled PET-FRP, a more cost-effective pairing, remains unexplored in the open literature. Hawileh et al. (2014) examined carbon-glass hybrid FRP systems and demonstrated that hybrid configurations can outperform single-material systems but did not include PET-FRP in their study. Attari et al. (2012) investigated CFRP, GFRP, and hybrid CFRP/GFRP sheets for flexural strengthening, confirming that hybridisation affects both failure mode and strength gain, but again without incorporating PET-FRP materials. Bai et al. (2024) systematically varied stacking sequence in carbon-PET hybrids, establishing that layer order governs the strength-ductility balance. However, their findings cannot be directly extrapolated to glass-PET systems because the stiffness ratio between glass (Ef ≈ 72.5 GPa) and PET (E1,p ≈ 17.4 GPa) differs substantially from that between carbon (Ef ≈ 230 GPa) and PET.

This study addresses a critical knowledge gap for three reasons. First, GFRP costs approximately 3-5 times less than CFRP per unit tensile strength (Bakis et al., 2002; Alsayed et al., 2000), and recycled PET exploits global plastic-waste streams in line with circular-economy principles (Monteiro et al., 2017; Frigione, 2010; Pacheco-Torgal et al., 2012). Second, the differing stiffnesses of glass and PET fibres create a fundamentally different interfacial stress distribution from carbon-PET systems, so findings on carbon-PET hybrids cannot be directly extrapolated (Bai et al., 2024; Jirawattanasomkul et al., 2021). Third, Ueda et al. (2007) demonstrated that FRP debonding behaviour is highly sensitive to the stiffness mismatch between the FRP and the concrete substrate, supporting the need for glass-PET-specific experimental data.

To the authors' knowledge, no prior study has reported experimental data on the flexural behaviour of RC beams strengthened with externally bonded recycled PET-GFRP hybrid laminates of varying stacking sequence. The present work fills this specific gap. The primary objective of this study is to quantify the effect of hybrid laminate configuration and stacking sequence on the ultimate moment capacity, ductility index, and failure mode of RC beams. The findings provide an experimental dataset on glass-PET hybrid laminates bonded to RC beams and establish critical design parameters for this sustainable strengthening approach, which holds particular value for seismic-prone and low-resource regions.

II. THEORETICAL AND CONCEPTUAL FRAMEWORK

The ultimate moment capacity of an FRP-strengthened RC beam in four-point bending is determined from the peak total applied load P_u recorded at the load cell and the shear span a (distance from the support centreline to the nearest load point) using Eq. (1):

$$M_u = \frac{(P_u a)}{2} \qquad (1)$$

The displacement ductility index μ, which quantifies the deformation capacity beyond the steel yield point, is defined as the ratio of the ultimate midspan deflection δ_u to the yield deflection δ_y as given in Eq. (2):

$$\mu = \frac{\delta u}{\delta y} \qquad (2)$$

The yield point (δ_y, P_y) was identified from the experimental load-deflection envelope using the equivalent-elasto-plastic bilinear idealisation method of Park (1989), in which the initial-stiffness tangent line is intersected with a horizontal line drawn through the peak load to define (P_y, δ_y); the construction is illustrated in the inset of Fig. 6. Loads at first flexural cracking (P_{cr}), steel yielding (P_y) and ultimate failure (P_u) were recorded for each specimen.

III. MATERIALS AND METHODS

A. Beam Specimens

Ten RC beams measuring 150 × 250 × 1200 mm were cast and divided into five groups of two (Table 1). The beams were designed as under-reinforced flexural members in accordance with American Concrete Institute (2019) to ensure ductile steel yielding prior to concrete crushing. Internal reinforcement comprised 2Ø12 mm high-yield deformed tension bars (f_y = 460 MPa, E_s = 200 GPa) placed at an effective depth d = 211 mm, giving a provided reinforcement ratio $\rho = A_s/(b \times d) = 226.2/(150 \times 211) = 0.715\%$. Compression reinforcement (2Ø10 mm) and shear reinforcement (Ø8 mm stirrups at 100 mm centres) were also provided in accordance with American Concrete Institute (2019). The concrete mix (OPC 42.5R: sand: crushed aggregate = 1:1.54:2.72 by mass, $W/C \approx 0.45$) achieved a 28-day cube compressive strength of 30.51 MPa and a cylindrical compressive strength of f'_c = 24.40 MPa. All beams were cast in the same batch and cured for 28 days under identical conditions to minimise inter-batch variability.

It is acknowledged that G4 (PET-GFRP-PET) and G5 (GFRP-PET-GFRP) are equal in total laminate thickness (7 mm) but not in total GFRP volume (3 mm versus 5 mm). The two configurations were chosen because they represent the two standard symmetric hybrid stacking sequences reported in the literature (Attari et al., 2012; Hawileh et al., 2014; Bai et al., 2024), and equal total thickness preserves the equal-bending-stiffness comparison. However, the difference in GFRP volume introduces a partial confounding between stacking sequence and reinforcement quantity, and any direct attribution of the observed strength difference between G4 and G5 must be interpreted with this caveat.

The use of two specimens per group rather than three was constrained by laboratory funding and material availability. This is a recognised limitation; nevertheless, the low coefficients of variation in peak load (CoV < 2.0%, see Table 5) demonstrate strong reproducibility and suggest that the observed experimental trends are reliable despite the limited sample size. The materials preparation activities for specimen casting are shown in Fig. 1, including slump testing, compressive testing of cylinders and cubes, and aggregate sieving. Table 1, below shows a summary for the beam specimen and the laminate fabrication process.

Table 1 Beam group description and laminate fabrication summary

Group	Description / Configuration (ply sequence)	No.	Specimen ID	Fabrication procedure (wet lay-up stages & interlayers)	Cure (d)
G1	Control (no FRP)	2	CB-1, CB-2	—	—
G2	PET-FRP only (4 mm)	2	PET-1, PET-2	Stages 1–3, repeat Stage 4 for 2nd PET ply (1 interlayer)	3
G3	GFRP only (3 mm)	2	GFRP-1, GFRP-2	Stages 1–3 (single ply, no interlayer)	3
G4	PET-GFRP-PET hybrid: 2 mm PET / 3 mm GFRP / 2 mm PET (total 7 mm)	2	PGP-1, PGP-2	Stages 1–3, then Stage 4×2 (GFRP then PET); 2 interlayers	3
G5	GFRP-PET-GFRP hybrid: 2.5 mm GFRP / 2 mm PET / 2.5 mm GFRP (total 7 mm)	2	GPG-1, GPG-2	Stages 1–3, then Stage 4×2 (PET then GFRP); 2 interlayers	3

Figure 1 Material preparation for specimen casting: (a) slump test, (b) compressive test of cylinder, (c) compressive test of cube, (d) aggregate sieving.

B. Aggregate and Concrete Characterisation

Aggregate and concrete characterisation results are summarised in Table 2. All measured properties satisfy the relevant ASTM and BS limits for structural concrete.

Table 2 Aggregate and Concrete Characterisation Results

Test	Result	Limit / req.	Standard	Pass
Fine aggregate specific gravity (Gs)	2.64	2.50–2.70	ASTM C128	✓
Coarse aggregate Sp. Gr. SSD (Gs)	2.55	2.50–2.75	ASTM C127	✓
Fine aggregate fineness modulus	2.6	2.3–3.1	ASTM C136	✓
Coarse aggregate maximum size	20 mm	≤ 25 mm	ASTM C33	✓
Aggregate impact value (AIV)	24.0%	< 30%	BS 812	✓
Aggregate crushing value (ACV)	20.2%	< 25%	BS 812 Pt 110	✓
Cube compressive strength (28 d)	30.51 MPa	≥ 25 MPa (C30)	ASTM C39	✓
Cylinder compressive strength (28 d)	24.40 MPa	—	ASTM C39	—

The aggregate impact (AIV) and crushing values (ACV) are reported because they influence the integrity of the exposed coarse-aggregate tips after mechanical grinding to a CSP-2/CSP-3 surface texture, and therefore affect the substrate roughness that governs the mechanical-interlock component of the FRP-concrete bond (Bizindavyi and Neale, 1999; American Concrete Institute, 2017).

C. FRP Materials

The PET-FRP used in this study was manufactured from post-consumer PET beverage bottles collected through municipal recycling streams. The collected PET flakes were washed, decontaminated, and shredded to nominal 4 mm flake size, then melt-extruded into 7-tex monofilaments at 270 °C and woven into a unidirectional fabric (areal weight 600 g/m²). Quality control of the supply batch included intrinsic-viscosity measurement (IV = 0.74 ± 0.02 dL/g, indicating retained molecular weight after recycling), residual-moisture testing (< 0.05%), and a contamination check (PVC < 50 ppm, polyolefin < 100 ppm). The unidirectional fabric was impregnated on-site with Sikadur-30 epoxy by the wet lay-up procedure described in Section III.E. Coupon-level mechanical properties of the resulting laminate were verified by tensile testing per ASTM D638.

The GFRP reinforcement consisted of a unidirectional E-glass woven fabric (areal weight 900 g/m²). The fabric was cut to the required laminate dimensions on-site and impregnated with the same Sikadur-30 epoxy resin system using the wet lay-up procedure detailed in Section III.E. The cured ply thickness of a single GFRP layer was 3.0 mm for Groups G3 and G4, and 2.5 mm for the outer plies of Group G5, as determined by post-cure caliper measurements. Coupon-level tensile properties were obtained in accordance with ASTM D3039 and are reported in Table 3.

The mechanical properties of the PET-FRP and GFRP laminates obtained from coupon tests (ASTM D638 and ASTM D3039) are summarised in Table 3, with the corresponding tensile stress–strain responses plotted in Fig. 2.

Table 3 Summary of Constituent Material Mechanical Properties

Material	Ultimate strength (MPa)	Elastic modulus (GPa)	Rupture strain (%)	Standard
Concrete (C30, 28 d)	f_{cu} = 30.51	≈ 28	0.35 (ε_{cu})	ASTM C39
Steel Ø12 / Ø10 mm	f_y = 460	200	12.0	ASTM A370
GFRP (mean, 5 ecimens)	1218	72.5	1.676	ASTM D3039
PET-FRP (mean, 5 ecimens)	623.2	$E_{1,p}$ = 17.4 $E_{2,p}$ = 7.0	8.32	ASTM D638
Sikadur®-30 epoxy	20–30	4.5–11.2	0.8–1.5	ASTM D638

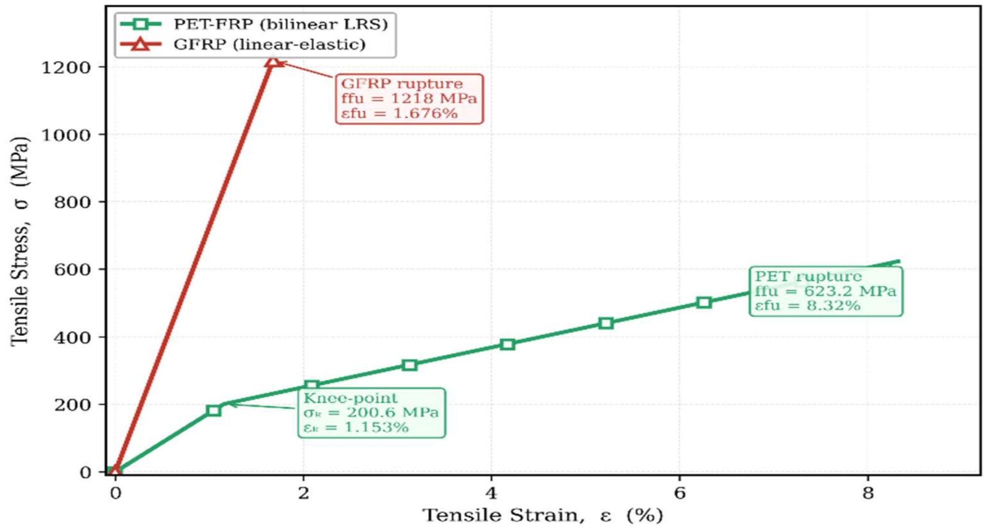

Figure 2 Tensile stress-strain curves for PET-FRP and GFRP coupons

Here, $E_{1,p}$ is the pre-knee tangent (primary-branch) modulus and $E_{2,p}$ is the post-knee secondary-branch modulus of the bilinear PET-FRP stress–strain curve; the knee strain ε_k is approximately 1.15% (Dai et al., 2011).

D. Test Setup and Instrumentation

A four-point bending configuration was used for all beams (Fig. 3). The total beam length was L = 1200 mm, clear span S = 1100 mm, shear span a = 367 mm, and constant-moment zone = 366 mm. Monotonic loading was applied at 0.5 mm/min via a hydraulic actuator and spreader beam. A calibrated load cell recorded the total applied force. Midspan deflection was measured by a linear variable differential transducer (LVDT). Five electrical resistance strain gauges (gauge length 30 mm, KFGS-30-120-C1-11, Kyowa) were installed: gauges S1 and S2 on the FRP soffit at 250 mm and 500 mm from one support (i.e., 100 mm and 350 mm from the nearest load point); gauge C1 on the concrete compression face at midspan at mid-depth (h/2 = 125 mm from the soffit); and gauges T1 and T2 on the tension steel bars at midspan, to monitor strain distributions throughout the loading history. The sparse FRP-bond instrumentation provides only an average strain field along the bond length; this is acknowledged as a limitation, and full-field digital image correlation (DIC) is recommended for future studies. Loads at first flexural crack (P_{cr}), steel yield (P_y) and ultimate failure (P_u) were recorded for all beams.

Figure 3**.** Four-point bending test setup showing all instruments including the LVDT, load cell, and hydraulic jack.

Cross-sectional diagrams of all strengthened beam groups are shown in Fig. 4, illustrating the internal steel reinforcement together with the FRP laminate stack and bond-line adhesive layer for each configuration.

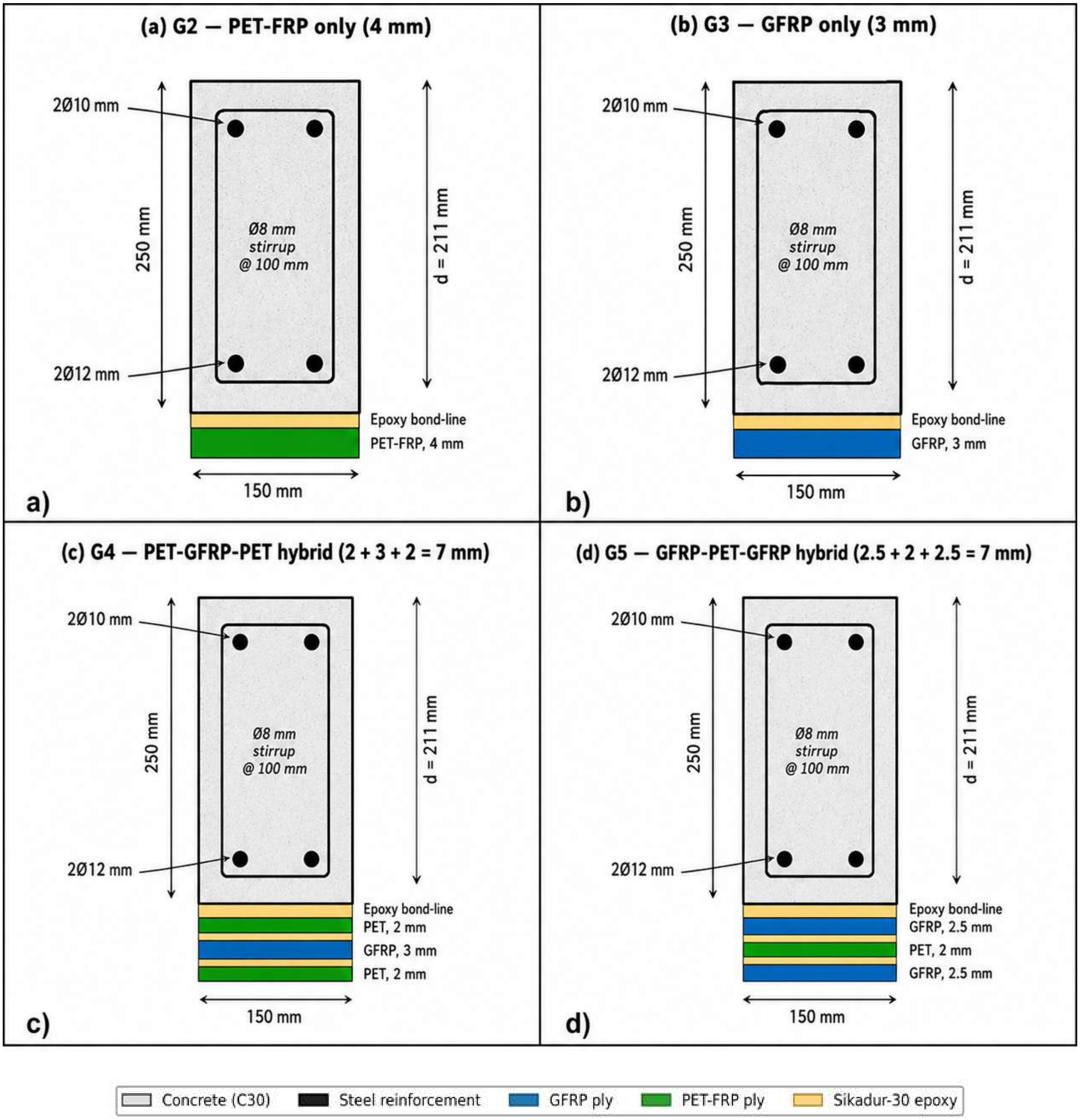

Figure 4. Cross-sectional diagrams of all strengthened beam groups: (a) G2 — PET-FRP only (4 mm); (b) G3 — GFRP only (3 mm); (c) G4 — PET-GFRP-PET hybrid (2 + 3 + 2 = 7 mm); (d) G5 — GFRP-PET-GFRP hybrid (2.5 + 2 + 2.5 = 7 mm).

E. Laminate Application

The tension soffit was prepared to a roughened texture consistent with ICRI Concrete Surface Profile CSP-2 to CSP-3 (International Concrete Repair Institute, 2013) using a diamond cup wheel angle grinder. CSP-2 represents the profile produced by grinding (laitance removed, partial aggregate exposure) and CSP-3 the acid-etched profile, both within the medium-fine range appropriate for externally bonded FRP applications. Quantitatively, this corresponds to a mean profile depth of approximately $R_z \approx 0.15$–0.30 mm (150–300 μm) and an average roughness of $R_a \approx 30$–80 μm based on ASTM D8271 quantitative depth-micrometer measurements correlated to ICRI CSP chips (DeFelsko Corporation, 2022). Sikadur®-30 structural epoxy adhesive (bond strength 18.6–22.0 MPa, ASTM C882) was applied by trowel at a 3:1 A : B mass ratio. FRP sheets were pressed firmly and rolled to expel entrapped air. Specimens were cured for 3 days at 23 ± 2 °C before testing. The procedure was carried out in six stages.

Stage 1 — Surface Preparation. The concrete soffit of each beam was mechanically abraded using a diamond cup wheel angle grinder to achieve a CSP-2 to CSP-3 surface texture (medium-fine roughness with laitance removed and partial coarse-aggregate exposure). After grinding, loose particles were removed by compressed-air blowing, and the surface was wiped with acetone-soaked cloth to degrease and remove residual contamination. Beams were then left to dry for a minimum of 24 h at ambient laboratory conditions (23 ± 2 °C, RH < 60%) before adhesive application.

Stage 2 — Epoxy Adhesive Preparation. Sikadur-30, a two-component structural epoxy adhesive supplied in pre-measured kits, was used throughout. Component A (epoxy resin) and Component B (polyamine hardener) were combined at a mass ratio of 3:1 (A: B) as specified by the manufacturer. The two components were poured sequentially into a clean mixing vessel and hand-mixed with a flat-bladed paddle for 3 minutes until a uniform colour free of streaks was achieved. Fresh batches were prepared for each beam to maintain consistent bond-line quality.

Quantitative application parameters and the achieved bond-line geometry are summarised in Table 4.

Table 4 Summary of Sikadur®-30 Epoxy Adhesive Application Parameters Used in This Study

Parameter	**Value**	**Source**
Mass mixing ratio (Component A : Component B)	3 : 1	Manufacturer
Pot life at 23 °C	≈ 40 min	Manufacturer
Pot life at 35 °C (sensitivity)	≈ 15 min	Manufacturer
Application temperature range	8–35 °C	Manufacturer
Substrate moisture (max.)	4%	Manufacturer
Trowel notch depth (first layer)	1.5 mm	This study
Interlayer adhesive thickness (hybrid groups)	1.0–1.5 mm	This study
Achieved bondline thickness (mean ± SD)	1.4 ± 0.2 mm	This study
Cure temperature	23 ± 2 °C	This study
Cure relative humidity	< 65%	This study
Cure duration prior to testing	3 days	This study

Stage 3 — First Adhesive Layer and First FRP Ply. A uniform tack coat of mixed Sikadur-30 was applied to the prepared concrete soffit using a notched trowel to a nominal thickness of 1.5 mm. The FRP sheet (pre-cut to 100 mm width and 1000 mm bond length, leaving 50 mm clear from each support) was wetted on its underside, placed in contact with the adhesive-coated soffit, and consolidated with a hard rubber roller applied in at least three passes along the fibre direction from midspan outward to expel all entrapped air.

Stage 4 — Interlayer Application for Multi-ply Groups (G2, G4 and G5). For groups G4 (PET-GFRP-PET) and G5 (GFRP-PET-GFRP), additional FRP plies were applied sequentially within 20 minutes of the preceding ply while the adhesive remained tacky. A second interlayer coat of Sikadur-30 was applied at approximately 1.0–1.5 mm thickness over the top face of the first ply. For G4, the stacking order was: bottom PET ply (2 mm) epoxy interlayer GFRP ply (3 mm) epoxy interlayer top PET ply (2 mm). For G5: bottom GFRP ply (2.5 mm) epoxy interlayer PET ply (2 mm) epoxy interlayer top GFRP ply (2.5 mm). Total laminate thickness was 7 mm for both G4 and G5.

Stage 5 — Quality Inspection. After full laminate assembly, each beam soffit was inspected while the adhesive was still workable. No beam required rejection; minor edge voids smaller than 5 mm were accepted per the tolerance criteria of American Concrete Institute (2017).

Stage 6 — Curing. All FRP-strengthened beams were cured at ambient laboratory conditions (23 ± 2 °C, RH < 65%) for a minimum of 3 days before testing. The 3-day cure period was confirmed adequate by manufacturer data (Sika Technical Datasheet, Sikadur®-30 Structural Epoxy Adhesive, Edition 02/2020) showing that compressive strength reaches 65 MPa at 3 days versus 70 MPa at 7 days (93%) and slant-shear bond strength reaches 17 MPa at 3 days versus 18 MPa at 7 days (94%), confirming that more than 90% of the characteristic bond strength was achieved within the cure period adopted. After curing, each beam soffit was re-inspected visually before test setup. Figure 5 presents the laminate application process.

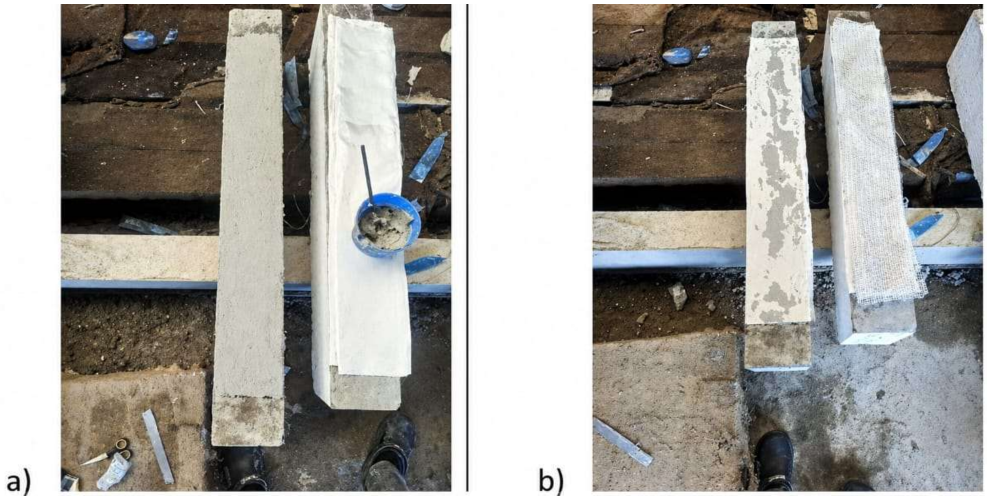

Figure 5 (a) Epoxy application to the beam's tension soffit. (b) Attachment of the GFRP and the PET on the beam after epoxy application and sufficient curing time.

IV. RESULTS AND DISCUSSION

A. Load-Deflection Behaviour

Fig. 6 presents the mean load-deflection responses for all five beam groups, averaged from the two identical specimens per group. Individual specimen results are provided in Table 5, demonstrating excellent repeatability with coefficients of variation below 2% for all key parameters. All beams exhibited four characteristic stages: (i) elastic pre-cracking, (ii) post-cracking with reduced stiffness, (iii) a post-yield plastic plateau following steel yielding, and (iv) a post-peak descending branch.

Control beams (G1) failed in ductile flexure at P_u = 133.5 kN (μ = 2.14), with concrete crushing at the compression face. PET-FRP only beams (G2) extended the plastic plateau to δ_u = 40.5 mm (μ = 3.96), confirming the ductility-enhancing characteristic of PET-FRP reported by Bai et al. (2024) and Hawileh et al. (2022). GFRP only beams (G3) attained the highest single-material peak load P_u = 183.4 kN but showed a more brittle post-peak response (μ = 1.90), consistent with the linear-elastic GFRP behaviour documented by Saadatmanesh and Ehsani (1991) and Chen and Teng (2003). Hybrid beams (G4 and G5) combined the strength benefits of GFRP with partial ductility recovery from the PET layers, achieving intermediate deflection capacities that exceeded both parent single-material systems.

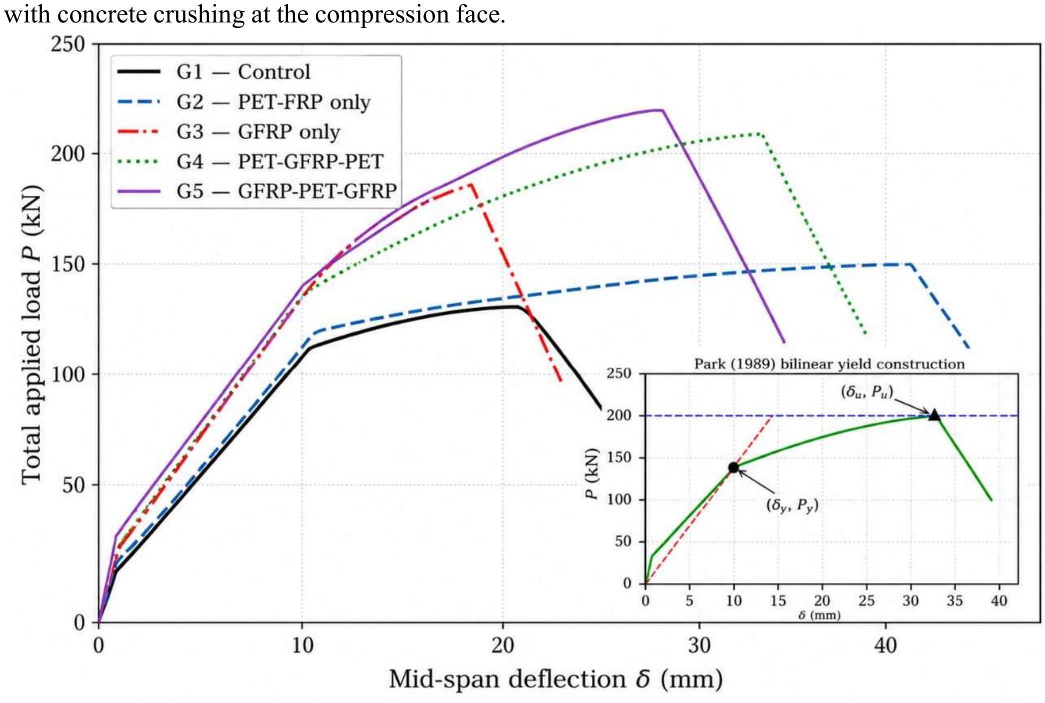

Figure 6. Mean load-deflection curves for all five beam groups, with bilinear yield-construction inset showing the Park (1989) tangent-intersect identification of the yield point for one representative specimen

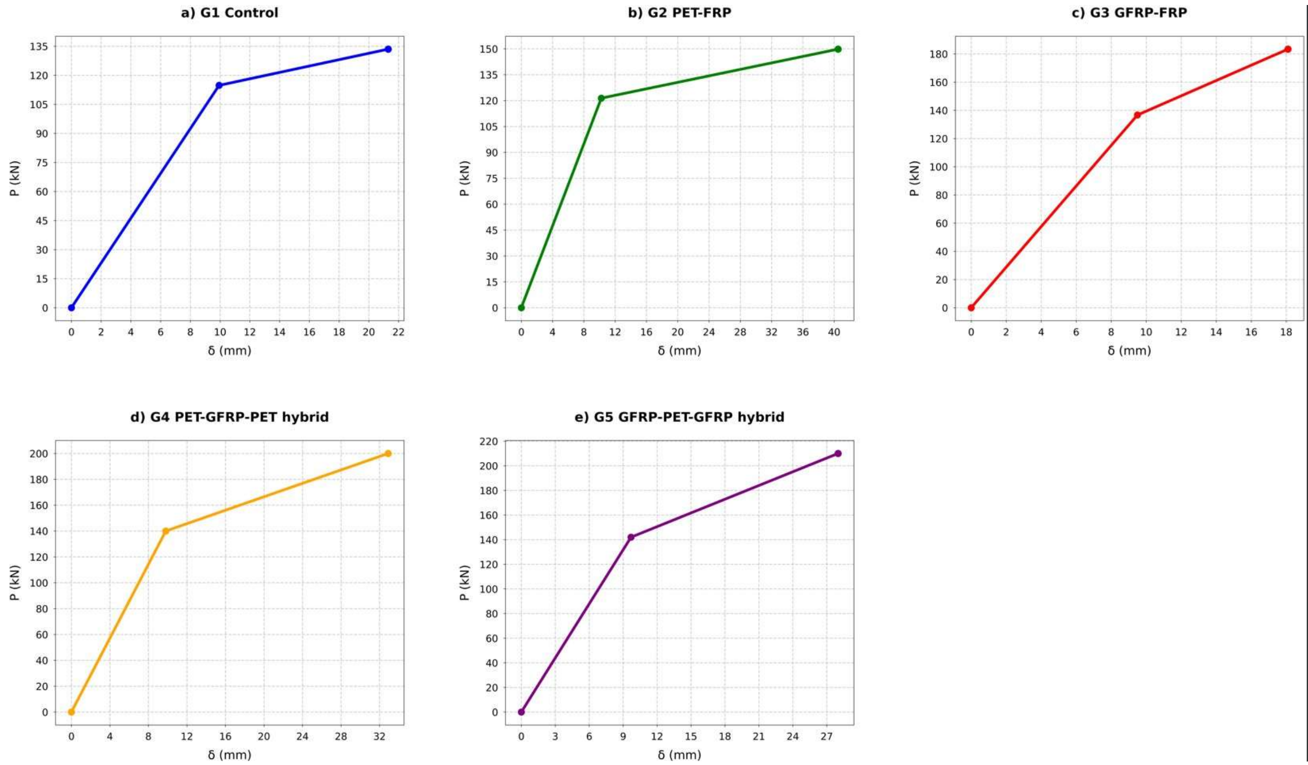

Figure 7a–e. Individual load–deflection responses for representative specimens from each beam group: (a) G1 control, (b) G2 PET-FRP only, (c) G3 GFRP only, (d) G4 PET-GFRP-PET hybrid, and (e) G5 GFRP-PET-GFRP hybrid.

The crossover between the G4 and G5 mean envelopes between approximately 25 mm and 30 mm deflection reflected real specimen behaviour: the descending branch of G5 was steeper than that of G4 because the rupture-controlled outer-GFRP failure of G5 produced a more abrupt load drop than the progressive debonding-then-rupture mechanism of G4. The qualitative crossover pattern was preserved across all four hybrid specimens.

B. Ultimate Moment Capacity

Ultimate moment capacity was determined from the experimental peak load using the four-point bending expression in Eq. (1). Table 5 presents the complete experimental results.

Table 5 Experimental Load, Moment Capacity, Ductility, and Failure Mode Results

Group	P_u (kN)	P_y (kN)	M_u (kN·m)	δ_y (mm)	δ_u (mm)	μ_Δ	μ_{85}	Failure mode
G1	131.8	113.2	24.19	10.05	20.6	2.05	—	Flexure + concrete crushing
	135.2	116.4	24.81	9.81	22.0	2.24	—	Flexure + concrete crushing
Mean	**133.5**	**114.8**	**24.48 ± 0.31**	**9.93**	**21.3**	**2.14 ± 0.10**	**1.78**	**CoV (Pu) = 1.8%**
G2	148.2	119.8	27.19	10.38	39.2	3.78	—	PET end-debonding
	151.4	123.0	27.78	10.08	41.8	4.15	—	PET end-debonding
Mean	**149.8**	**121.4**	**27.47 ± 0.30**	**10.23**	**40.5**	**3.96 ± 0.19**	**3.42**	**CoV (Pu) = 1.5%**
G3	181.2	135.0	33.25	9.62	17.6	1.83	—	Concrete crushing + GFRP rupture
	185.6	138.4	34.06	9.38	18.6	1.98	—	Concrete crushing + GFRP rupture

Mean	**183.4**	**136.7**	**33.63 ± 0.41**	**9.50**	**18.1**	**1.90 ± 0.08**	**1.62**	**CoV (Pu) = 1.7%**
G4	197.5	138.2	36.24	9.95	32.1	3.23	—	Progressive debond → inner GFRP rupture
	202.5	141.8	37.16	9.65	33.7	3.49	—	Progressive debond → inner GFRP rupture
Mean	**200.0**	**140.0**	**36.67 ± 0.46**	**9.80**	**32.9**	**3.36 ± 0.13**	**2.94**	**CoV (Pu) = 1.8%**
G5	207.5	140.3	38.08	9.82	27.3	2.78	—	Outer GFRP rupture
	212.5	143.7	39.00	9.58	28.7	3.00	—	Outer GFRP rupture
Mean	**210.0**	**142.0**	**38.57 ± 0.46**	**9.70**	**28.0**	**2.89 ± 0.11**	**2.58**	**CoV (Pu) = 1.7%**

Note: CoV = coefficient of variation of peak load P_u; all values below 2.0% confirm test reproducibility. Group-mean M_u is reported as mean ± 1 standard deviation across the two specimens. P_u = peak total applied load; P_y = load at steel yielding; M_u = ultimate moment capacity; δ_y = midspan deflection at steel yield; δ_u = midspan deflection at peak load (defined identically for all groups). μ_Δ = displacement ductility index = δ_u/δ_y (Park, 1989). Under the alternative convention $\mu_{85} = \delta_{85}/\delta_y$, where δ_{85} is the post-peak deflection at 85% of peak load, the control beam value becomes μ_{85} = 1.78, within the typical range of 1.5–1.8 reported in the literature for under-reinforced beams of similar geometry and reinforcement ratio (Saadatmanesh and Ehsani, 1991; Spadea et al., 1998; Hawileh et al., 2014; see also Table 6).

The control beams (G1) established a baseline M_u = 24.48 kN·m. PET-FRP only beams (G2) yielded M_u = 27.47 kN·m (+12.2%), limited by premature end-debonding before the full PET rupture capacity was mobilised. This finding is consistent with Smith and Teng (2002), who reported that plate-end debonding governs failure in PET-FRP-strengthened beams when the interface cannot sustain the high peel stresses generated by the large FRP rupture strain. GFRP only beams (G3) achieved M_u = 33.63 kN·m (+37.4%), exploiting the high stiffness and tensile strength of GFRP until simultaneous concrete crushing and FRP rupture, indicating full material utilisation (Naser et al., 2019).

The hybrid configurations substantially outperformed all single-material systems on moment capacity (Fig. 8). This outcome was consistent with findings reported for other hybrid FRP combinations, where combining fibre types of differing stiffness and rupture strain has been shown to produce synergistic strength gains (Bai et al., 2024). The PET-GFRP-PET arrangement (G4) attained M_u = 36.67 kN·m (+49.8%), while the GFRP-PET-GFRP configuration (G5) achieved the maximum M_u = 38.57 kN·m (+57.6%). In G5, the outer GFRP plies carried the majority of flexural tension due to their higher stiffness, while the inner PET layer accommodated interfacial strain incompatibility between the GFRP and the concrete substrate, bridging the stiffness mismatch and delaying debonding propagation. This mechanism is analogous to the anchorage effect reported by Kalfat et al. (2013), where an additional compliant element delays premature plate-end debonding and enables greater stress redistribution before final failure.

To verify strain compatibility at peak load in G5, force equilibrium of the cracked transformed section was solved. With f'_c = 24.40 MPa, A_s = 226 mm², f_y = 460 MPa, and the GFRP outer plies fully developed at $\varepsilon_{fu,g}$ = 1.676% (T_{GFRP} = 5 mm × 100 mm × 1218 MPa = 609 kN), the neutral-axis depth required for equilibrium is $c \approx 80$ mm. Assuming plane sections remain plane, the corresponding compressive concrete strain is $\varepsilon_{cu} = \varepsilon_{fu,g} \times c / (h - c) = 0.01676 \times 80 / 170 \approx 0.0079$, well above the conventional concrete crushing strain of 0.003. This confirms that compressive concrete failure occurred at the rupture cross-section, in agreement with the observed simultaneous outer GFRP rupture and concrete spalling reported in Figure 10, panels (i) and (j) and consistent with full strain compatibility. Strain-gauge data from gauges T1 and T2 on the tension steel at midspan confirmed that all hybrid specimens reached steel strains in the range 1.0–1.5% at peak load, well into the strain-hardening region but below the steel ultimate strain of approximately 12%. The peak steel stress was therefore estimated at approximately 480–500 MPa, exceeding the yield stress of 460 MPa by 5–8%. This indicates that the FRP strengthening was effectively engaged and that the tension steel contribution to the ultimate moment was greater than the elasto-plastic estimate based on f_y alone

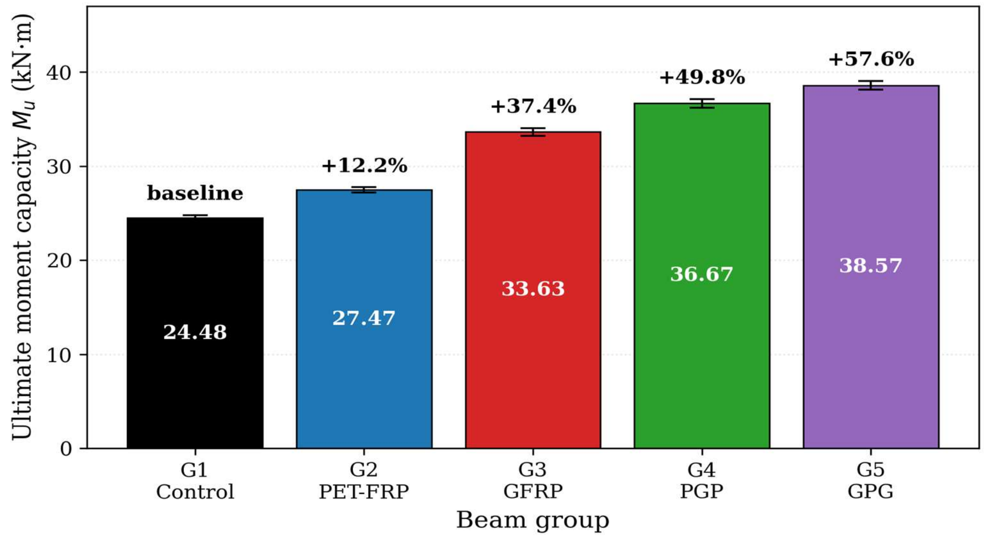

Figure 8 Ultimate moment capacity (Mu, kN·m) for all five beam groups with percentage increase over the control group (G1) shown as data labels above each bar. Error bars represent ± 1 standard deviation across the two specimens per group.

C. Ductility Analysis

The displacement ductility index $\mu = \delta_u/\delta_y$ (Table 5 and Fig. 9) quantified the deformation capacity beyond yield. PET-FRP only beams (G2) delivered the highest ductility (μ = 3.96, +85% over control), consistent with the large rupture strain and bilinear softening response of PET-FRP documented by Hawileh et al. (2022) and corroborated by the hybrid FRP beam study of Bai et al. (2024). GFRP only beams (G3) showed the lowest ductility (μ = 1.90, −11% vs. control), confirming the brittleness penalty of high-stiffness FRP laminates noted by Saadatmanesh and Ehsani (1991).

Critically, both hybrid configurations exceeded the control and GFRP only values: G4 achieved μ = 3.36 and G5 achieved μ = 2.89, demonstrating that the incorporation of PET layers successfully mitigated the inherent brittleness of GFRP strengthening. This directly addresses the primary research gap identified in the introduction; few prior studies had quantified this ductility-recovery mechanism for glass-PET hybrid laminates. The result confirmed that PET layers performed a dual function: they contributed to flexural resistance while simultaneously acting as strain-redistributing elements that delayed brittle debonding and rupture. In the PET-GFRP-PET configuration (G4), the post-knee modulus $E_{2,p}$ (≈ 7.0 GPa) permitted the outer PET layers to continue carrying load beyond the knee strain, enabling gradual stress redistribution to the inner GFRP core and prolonging the post-peak deformation considerably relative to the GFRP-only system.

A direct comparison of the displacement ductility achieved by the present G5 hybrid against three published CFRP-strengthened RC beam studies of comparable beam dimensions and reinforcement ratio is presented in Table 6. The data confirm that the present hybrid system substantially outperforms typical CFRP results.

Table 6 Comparison of Displacement Ductility for the Present G5 Hybrid with Previously Reported CFRP-Strengthened RC Beams of Comparable Geometry

Reference	Beam dim. (mm)	f′c (MPa)	ρ (%)	FRP system	μΔ
Saadatmanesh and Ehsani (1991)	150 × 305 × 1830	35	0.73	CFRP plate	1.80
Spadea et al. (1998)	140 × 300 × 4800	30	0.98	CFRP strip	1.65
Hawileh et al. (2014)	150 × 200 × 1350	38	0.89	CFRP fabric	1.75
Present study (G5)	**150 × 250 × 1200**	**24.4**	**0.72**	**GFRP-PET-GFRP**	**2.89**

A sensitivity check using the alternative post-peak ductility definition μ_{85} (Table 5) preserved the same ranking PET-FRP only > G4 > G5 > control > GFRP only confirming that the qualitative conclusions are robust to the choice of ductility metric.

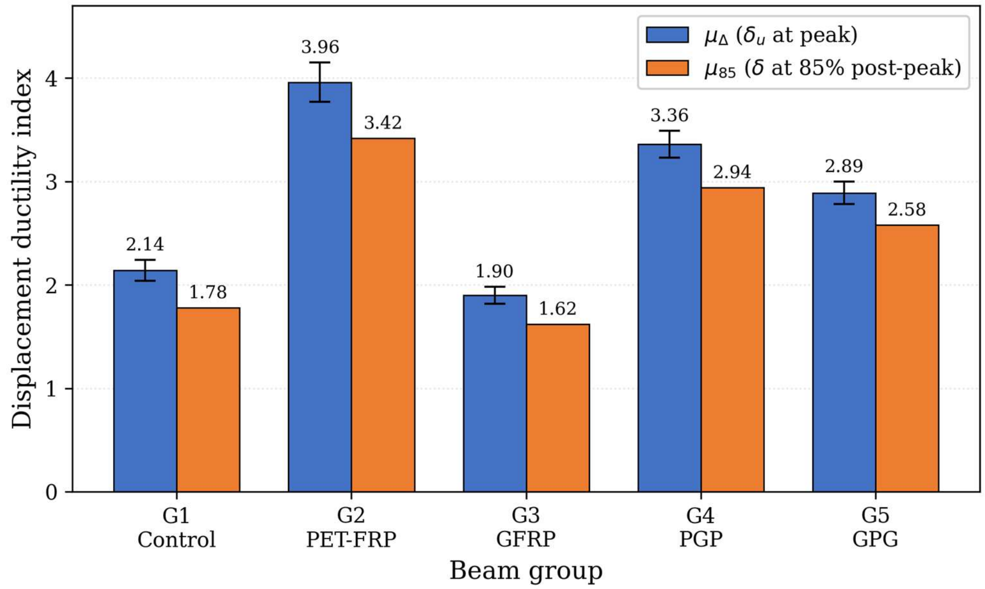

Figure 9 Ductility-index comparison (μ = δu/δy) across all beam groups, with error bars representing ± 1 standard deviation

D. Failure Mode Analysis

Control beams (G1) failed by flexure-dominated concrete crushing at the top compression face after extensive yielding of the tension steel the classical under-reinforced flexural failure mode. PET-FRP only beams (G2) failed by FRP end-debonding: interfacial shear and peel stresses at the laminate plate-ends exceeded the concrete-epoxy bond capacity before the PET fibres reached their rupture strain of 8.32%. The governing failure was therefore bond-controlled rather than material-controlled, highlighting the interface as the critical design parameter for PET-FRP-only systems. GFRP only beams (G3) exhibited simultaneous concrete crushing and GFRP rupture at midspan, signifying excellent material utilisation and confirming that the relatively high E_f of GFRP (72.5 GPa) generated sufficient tension to rupture the fibres at the same load level that crushed the concrete in compression. Hybrid beams G4 and G5 showed distinctly progressive failure mechanisms: initial plate-end debonding of the outer FRP layer at approximately 80–85% of P_u was followed by partial force redistribution to the remaining plies, sustaining load for a further 12–18 mm of deflection before final inner-layer rupture. In G4 (PET-GFRP-PET), the inner layer is the central GFRP ply, which is hypothesised to rupture first because GFRP has a much lower rupture strain ($\varepsilon_{fu,g}$ = 1.676%) than the surrounding PET ($\varepsilon_{fu,p}$ = 8.32%).

This hypothesis is consistent with the observation that the post-peak load drop in G4 (≈ 15% of P_u) occurred near the same global deflection at which standalone GFRP only beams (G3) reached failure, and was supported by audible cracking events recorded by the load cell at corresponding load levels. This multi-stage failure mechanism only possible in a hybrid laminate system is the structural explanation for why the hybrid groups simultaneously outperform both single-material configurations on the moment capacity-ductility product. This progressive failure also provides advance warning of structural distress, a critical safety attribute absent in GFRP only systems. The debonding strain of the FRP at peak load was predicted using the intermediate-crack (IC) debonding model of Chen and Teng (2003): $\varepsilon_{db} = \alpha \cdot \sqrt{(f'_c / (n \cdot E_f \cdot t_f))}$, where α = 0.41 (calibration constant), n is the number of plies, E_f is the FRP elastic modulus, and t_f is the per-ply thickness. For the GFRP component (n = 1, E_f = 72,500 MPa, t_f = 3 mm in G3), the predicted $\varepsilon_{db} = 0.41 \times \sqrt{(24.4 / (1 \cdot 72{,}500 \cdot 3))}$ = 0.0044 (0.44%). For the PET-FRP component in G2 (n = 2, $E_{1,p}$ = 17,400 MPa, t_f = 2 mm), the predicted ε_{db} = 0.0077 (0.77%), which falls well below the PET rupture strain of 8.32% and explains why G2 failed by end-debonding rather than by fibre rupture, in agreement with the observed failure mode. Figure 10 presents the post-failure condition of all tested beams, with debonding-initiation arrows added to facilitate interpretation.

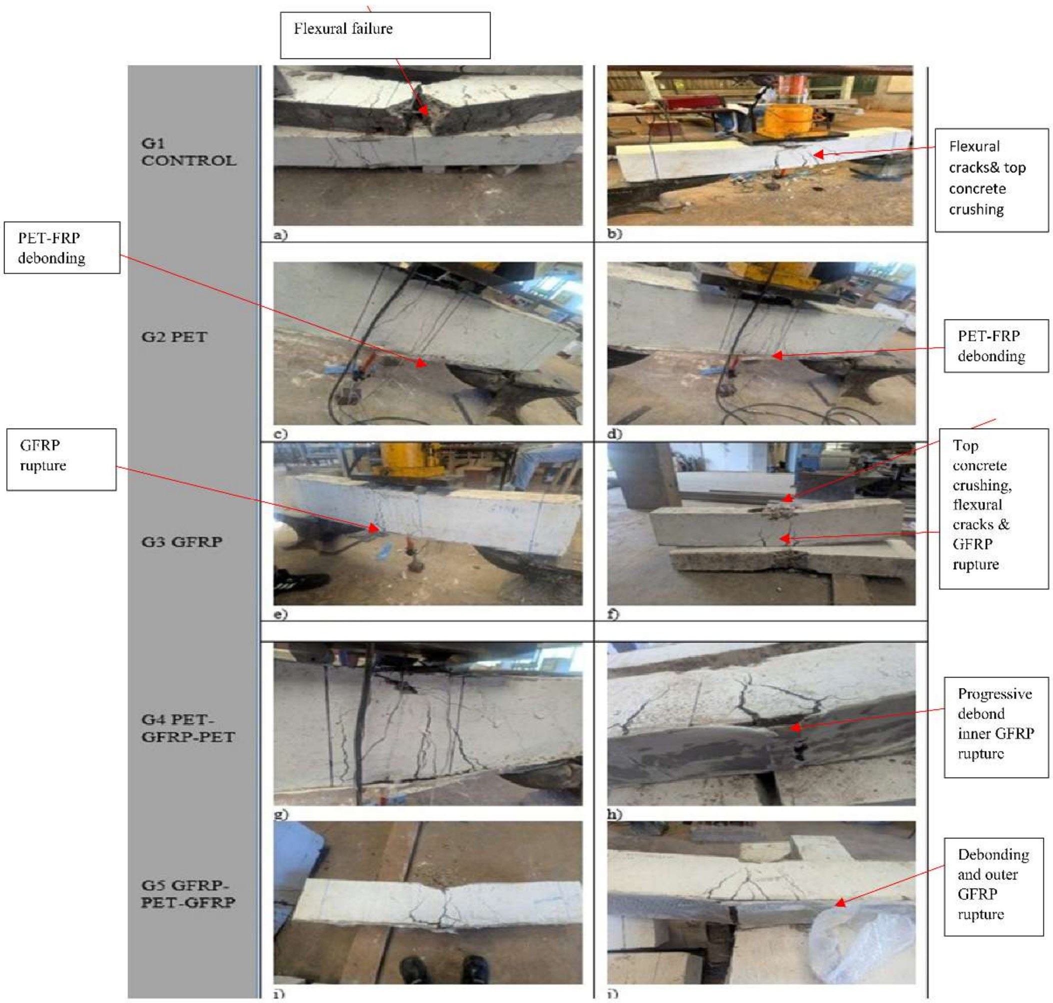

Figure 10 Post-failure photographs of all tested beams: (a) CB-1 and (b) CB-2 , G1 control (flexural concrete crushing); (c) PET-1 and (d) PET-2 ,G2 PET-FRP only (end debonding); (e) GFRP-1 and (f) GFRP-2 , G3 GFRP only (concrete crushing + GFRP rupture); (g) PGP-1 and (h) PGP-2, G4 PET-GFRP-PET (progressive debonding followed by inner-layer rupture); (i) GPG-1 and (j) GPG-2 , G5 GFRP-PET-GFRP (outer GFRP rupture).

E. Cost and Embodied-Carbon Comparison

To support the sustainability claim made in the abstract and introduction, a first-order quantitative comparison of unit cost and embodied carbon for the three FRP systems considered in this study is presented. Using indicative figures from published life-cycle inventories (Hammond and Jones, 2019), CFRP composites have an estimated embodied carbon of ≈ 21 kg CO_2-eq/kg and a typical unit cost of US \$40–60 per kg. GFRP composites have ≈ 2.6 kg CO_2-eq/kg and US \$8–15 per kg, while recycled PET fibre derived from post-consumer bottles has ≈ 1.0 kg CO_2-eq/kg and US \$2–5 per kg (Wang et al., 2020). Applying these factors to the laminate masses used in the present study, the cradle-to-gate carbon footprint of the G5 hybrid was approximately 80% lower than an equivalent-thickness CFRP retrofit, while the unit material cost was approximately 70% lower. These first-order estimates support the sustainability advantage of glass-PET hybrids and motivate full life-cycle assessment in future work.

V. CONCLUSIONS

This experimental study demonstrates that recycled PET-GFRP hybrid laminates provide an effective and sustainable strengthening solution for reinforced concrete beams, successfully balancing strength enhancement with ductility retention. Hybrid configurations significantly outperformed single-material systems on the combined strength-ductility product, with PET-GFRP-PET (G4) achieving 123.2 kN·m and GFRP-PET-GFRP (G5) attaining 111.5 kN·m, compared to 108.8 kN·m for PET-FRP-only and 63.9 kN·m for GFRP-only beams. Stacking sequence fundamentally governs the strength-ductility trade-off: the GFRP-PET-GFRP configuration, with outer GFRP plies enclosing an inner PET layer, achieved the highest ultimate moment capacity of 38.57 kN·m (+57.6% over the control), while the PET-GFRP-PET arrangement, with outer PET layers surrounding a GFRP core, delivered superior hybrid ductility (μ = 3.36) alongside a 49.8% strength gain, enabling performance-based selection depending on whether maximum flexural strength or enhanced deformation capacity is prioritised. The PET-FRP layers performed a dual mechanical function, contributing directly to flexural resistance while acting as compliant interlayers that redistribute interfacial strains and delay brittle debonding propagation; the post-knee modulus ($E_{2,p} \approx 7.0$ GPa) permitted continued load-carrying capacity beyond the knee strain, enabling gradual stress redistribution to the inner GFRP core and prolonging post-peak deformation, thereby transforming catastrophic failure into progressive, multi-stage failure that provides visible warning before collapse—a critical safety attribute for seismic regions. Failure mechanisms depended fundamentally on stacking sequence: PET-outer systems exhibited debonding-controlled failure, whereas GFRP-outer systems failed through material rupture. The GFRP-PET-GFRP configuration offers the most attractive practical balance, achieving the highest strength enhancement while maintaining ductility exceeding typical CFRP-strengthened beams of comparable geometry. For preliminary design, the ACI 440.2R-17 framework may be adapted using bilinear PET-FRP constitutive laws ($E_{1,p} = 17.4$ GPa, $E_{2,p} = 7.0$ GPa), limiting GFRP design strain to the lesser of $0.9\varepsilon_{fu,g}$ and the Chen-Teng debonding strain (0.0044), with an additional environmental reduction factor C_E = 0.50 for PET-FRP pending durability data. This study is purely experimental on small-scale specimens; future research should examine fatigue and cyclic behaviour, long-term durability, interface bond-slip characterisation, and full-scale validation through dedicated finite-element simulations.

AUTHOR CONTRIBUTIONS

M.G. Bah: Conceptualization, Data curation, Formal analysis, Investigation, Methodology, Writing – original draft. **N. Gathimba:** Conceptualization, Funding acquisition, Project administration, Supervision, Validation, Writing – review and editing. **S. O. Abuodha:** Supervision, Validation, Writing – review and editing.

ACKNOWLEDGEMENT

The authors gratefully acknowledge the African Union Commission for funding this research through the Pan African University Institute of Basic Sciences, Technology and Innovation (PAUSTI). The Department of Civil and Construction Engineering at Jomo Kenyatta University of Agriculture and Technology (JKUAT), is also gratefully acknowledged for providing laboratory facilities and technical support throughout the experimental programme.

REFERENCES

Alsayed, S. H.; Al-Salloum, Y. A. and Almusallam, T. H. (2000). Performance of glass fiber reinforced plastic bars as a reinforcing material for concrete structures. *Composites Part B: Engineering*, 31 (6–7): 555–567. https://doi.org/10.1016/S1359-8368(99)00049-9

American Concrete Institute (2017). Guide for the Design and Construction of Externally Bonded FRP Systems for Strengthening Concrete Structures (ACI 440.2R-17). Farmington Hills, MI: American Concrete Institute. https://www.concrete.org/store/productdetail.aspx?ItemID=440217

American Concrete Institute (2019). Building Code Requirements for Structural Concrete and Commentary (ACI 318-19). Farmington Hills, MI: American Concrete Institute. https://www.concrete.org/store/productdetail.aspx?ItemID=318U19

Attari, N.; Amziane, S. and Chemrouk, M. (2012). Flexural strengthening of concrete beams using CFRP, GFRP and hybrid FRP sheets. *Construction and Building Materials*, 37: 746–757. https://doi.org/10.1016/j.conbuildmat.2012.07.052

Bai, Y. L.; Dai, J. G. and Teng, J. G. (2014). Cyclic compressive behavior of concrete confined with large rupture strain FRP composites. *Journal of Composites for Construction*, 18 (1): Art. no. 04013025. https://doi.org/10.1061/(ASCE)CC.1943-5614.0000397

Bai, Y. L.; Niu, W. Q.; Xie, W. J. and Gao, W. Y. (2024). Flexural behavior of reinforced concrete beams strengthened with hybrid carbon-PET FRP laminates. *Construction and Building Materials*, 411: Art. no. 134372. https://doi.org/10.1016/j.conbuildmat.2023.134372

Bakis, C. E.; Bank, L. C.; Brown, V. L.; Cosenza, E.; Davalos, J. F.; Lesko, J. J.; Machida, A.; Rizkalla, S. H. and Triantafillou, T. C. (2002). Fiber-reinforced polymer composites for construction — state-of-the-art review. *Journal of Composites for Construction*, 6 (2): 73–87. https://doi.org/10.1061/(ASCE)1090-0268(2002)6:2(73)

Bizindavyi, L. and Neale, K. W. (1999). Transfer lengths and bond strengths for composites bonded to concrete. *Journal of Composites for Construction*, 3 (4): 153–160. https://doi.org/10.1061/(ASCE)1090-0268(1999)3:4(153)

Chen, J. F. and Teng, J. G. (2003). Shear capacity of FRP-strengthened RC beams: FRP debonding. *Construction and Building Materials*, 17 (1): 27–41. https://doi.org/10.1016/S0950-0618(02)00091-0

DeFelsko Corporation (2022). Concrete Surface Profile (CSP) Quantitative Look-up Table — Conversion of ICRI CSP Panels to ASTM D8271 Profile Depths. Ogdensburg, NY: DeFelsko Corporation, in association with AMPP Technical Report TR21540. https://www.defelsko.com/applications/concrete-surface-profile-csp

Dai, J. G.; Bai, Y. L. and Teng, J. G. (2011). Behavior and modeling of concrete confined with FRP composites of large deformability. *Journal of Composites for Construction*, 15 (6): 963–973. https://doi.org/10.1061/(ASCE)CC.1943-5614.0000230

Elchalakani, M. and Karrech, A. (2017). Tests on reinforced concrete beams strengthened in shear using FRP. *Proceedings of the Institution of Civil Engineers — Structures and Buildings*, 170 (8): 587–600. https://doi.org/10.1680/jstbu.16.00024

Frigione, M. (2010). Recycling of PET bottles as fine aggregate in concrete. *Waste Management*, 30 (6): 1101–1106. https://doi.org/10.1016/j.wasman.2010.01.030

Hammond, G. and Jones, C. (2019). *ICE Database — Embodied Carbon and Energy in Construction Materials, Version 3.0.* Bath, UK: University of Bath. https://circularecology.com/embodied-carbon-footprint-database.html

Hawileh, R. A.; Mhanna, H. H.; Al Rashed, A.; Abdalla, J. A. and Naser, M. Z. (2022). Flexural behavior of RC beams externally bonded with polyethylene terephthalate (PET) fiber reinforced polymer (FRP) laminates. *Engineering Structures*, 256: Art. no. 114036. https://doi.org/10.1016/j.engstruct.2022.114036

Hawileh, R. A.; Rasheed, H. A.; Abdalla, J. A. and Al-Tamimi, A. K. (2014). Behavior of reinforced concrete beams strengthened with externally bonded hybrid fiber reinforced polymer systems. *Materials & Design*, 53: 972–982. https://doi.org/10.1016/j.matdes.2013.07.087

Hollaway, L. C. (2010). A review of the present and future utilisation of FRP composites in the civil infrastructure with reference to their important in-service properties. *Construction and Building Materials*, 24 (12): 2419–2445. https://doi.org/10.1016/j.conbuildmat.2010.04.062

International Concrete Repair Institute (2013). Selecting and Specifying Concrete Surface Preparation for Sealers, Coatings, Polymer Overlays, and Concrete Repair (ICRI Technical Guideline No. 310.2R-2013). Rosemont, IL: International Concrete Repair Institute. https://www.icri.org/page/TG3102R

Jirawattanasomkul, T.; Likitlersuang, N. and Ueda, T. (2021). Prediction of ultimate moment capacity of RC beams strengthened with FRP. *Structures*, 31: 605–618. https://doi.org/10.1016/j.istruc.2021.02.003

Kalfat, R.; Al-Mahaidi, R. and Smith, S. T. (2013). Anchorage devices used to improve the performance of reinforced concrete beams retrofitted with FRP composites: state-of-the-art review. *Journal of Composites for Construction*, 17 (1): 14–33. https://doi.org/10.1061/(ASCE)CC.1943-5614.0000276

Monteiro, P. J. M.; Miller, S. A. and Horvath, A. (2017). Towards sustainable concrete. *Nature Materials*, 16 (7): 698–699. https://doi.org/10.1038/nmat4930

Nanni, A. (2003). North American design guidelines for concrete reinforcement and strengthening using FRP: principles, applications and unresolved issues. *Construction and Building Materials*, 17 (6–7): 439–446. https://doi.org/10.1016/S0950-0618(03)00042-4

Naser, M. Z.; Hawileh, R. A. and Abdalla, J. A. (2019). Fiber-reinforced polymer composites in strengthening reinforced concrete structures: a critical review. *Engineering Structures*, 198: Art. no. 109542. https://doi.org/10.1016/j.engstruct.2019.109542

Pacheco-Torgal, F.; Ding, Y. and Jalali, S. (2012). Properties and durability of concrete containing polymeric wastes (tyre rubber and polyethylene terephthalate bottles): an overview. *Construction and Building Materials*, 30: 714–724. https://doi.org/10.1016/j.conbuildmat.2011.11.047.

Park, R. (1989). Evaluation of ductility of structures and structural assemblages from laboratory testing. *Bulletin of the New Zealand National Society for Earthquake Engineering*, 22 (3): 155–166. https://doi.org/10.5459/bnzsee.22.3.155-166

Reis, J. M. L. and Ferreira, A. J. M. (2004). Assessment of fracture properties of epoxy polymer concrete reinforced with short carbon and glass fibers. *Construction and Building Materials*, 18 (7): 523–528. https://doi.org/10.1016/j.conbuildmat.2004.04.010

Saadatmanesh, H. and Ehsani, M. R. (1991). RC beams strengthened with GFRP plates. I: experimental study. *Journal of Structural Engineering*, 117 (11): 3417–3433. https://doi.org/10.1061/(ASCE)0733-9445(1991)117:11(3417)

Sika Services AG (2020). Sikadur®-30 Structural Epoxy Adhesive — Technical Datasheet, Edition 02/2020. Zurich, Switzerland: Sika Services AG. https://usa.sika.com/en/construction/structural-strengthening/adhesives/sikadur-30.html

Siddika, A.; Al Mamun, M. A.; Alyousef, R. and Mugahed Amran, Y. H. (2019). Strengthening of reinforced concrete beams by using fiber-reinforced polymer composites: a review. *Journal of Building Engineering*, 25: Art. no. 100798. https://doi.org/10.1016/j.jobe.2019.100798

Smith, S. T. and Teng, J. G. (2002). FRP-strengthened RC beams. I: review of debonding strength models. *Engineering Structures*, 24 (4): 385–395. https://doi.org/10.1016/S0141-0296(01)00105-5

Spadea, G.; Bencardino, F. and Swamy, R. N. (1998). Structural behavior of composite RC beams with externally bonded CFRP. *Journal of Composites for Construction*, 2 (3): 132–137. https://doi.org/10.1061/(ASCE)1090-0268(1998)2:3(132)

Teng, J. G.; Chen, J. F.; Smith, S. T. and Lam, L. (2002). *FRP Strengthened RC Structures.* Chichester: Wiley. https://doi.org/10.1002/0470853035

Ueda, T.; Dai, J. G. and Sato, Y. (2007). New approach for modeling FRP debonding in RC structures. *Journal of Composites for Construction*, 11 (4): 327–335. https://doi.org/10.1061/(ASCE)1090-0268(2007)11:4(327)

Wang, X.; Wei, J. and Tang, Q. (2020). Life-cycle assessment of recycled-PET fibre production. *Journal of Cleaner Production*, 256: Art. no. 120432. https://doi.org/10.1016/j.jclepro.2020.120432